Journal of Molecular Liquids 442 (2026) 129055

Contents lists available at ScienceDirect

Journal of Molecular Liquids

journal homepage: www.elsevier.com/locate/molliq

Mechanistic insights into toxic metal adsorption in multicomponent systems using graphene oxide membranes: kinetic, equilibrium, and reuse studies

Tauany de Figueiredo Neves [a,b], Cláudia Batista Lopes [b], Valmor Roberto Mastelaro [c], Renato Falcão Dantas [a], Carlos Manuel Silva [b,d,*], Patrícia Prediger [a,*]

[a] Limeira School of Technology, University of Campinas, PO Box 456, 13484-332 Limeira, SP, Brazil
[b] CICECO, Department of Chemistry, University of Aveiro, Campus Universitário de Santiago, 3810-193 Aveiro, Portugal
[c] São Carlos Institute of Physics, University of São Paulo, PO Box 369, 13566-590 São Carlos, SP, Brazil
[d] CERES, Department of Chemical Engineering, University of Coimbra, Faculty of Sciences and Technology, Rua Sílvio Lima, Polo II, 3030-790, Coimbra, Portugal

ARTICLE INFO

Keywords:
Complexation
Isotherm modeling
Kinetic modeling
Multilayer adsorption
Nanocomposite
Polyacrylonitrile membranes

ABSTRACT

In this study, a composite membrane based on hydrolyzed polyacrylonitrile (hPAN) coated with graphene oxide (GO) and poly(4-vinylpyridinium iodide) (PVPI), referred to as hPAN/$PVPI_3$/GO_3, was evaluated for the removal of Cr^{3+}, Cu^{2+}, and Pb^{2+} ions from multicomponent aqueous systems. Adsorption performance was assessed through kinetic and equilibrium studies, while post-adsorption characterization elucidated the underlying adsorption mechanisms. Batch adsorption experiments, conducted over 24 h at 298 K and pH 5.5 with initial concentrations of 10 mg L^{-1} for Cr^{3+} and Pb^{2+} and 20 mg L^{-1} for Cu^{2+}, yielded maximum adsorption loadings of 6.42 mg g^{-1}, 23.2 mg g^{-1}, and 29.6 mg g^{-1} for Cr^{3+}, Cu^{2+}, and Pb^{2+}, respectively. The experimental assays revealed selective adsorption behavior. Spectroscopic and microscopic analyses confirmed interactions between metal cations and electron-rich functional groups on the membrane surface, as well as the reduction of Cu^{2+} to Cu^{+}. The hPAN/$PVPI_3$/GO_3 membrane maintained high adsorption efficiency for Cr^{3+} and Pb^{2+} over five consecutive cycles, demonstrating strong reusability. These results underscore the potential of hPAN/$PVPI_3$/GO_3 as a promising material for the remediation of toxic metals from contaminated water, with performance comparable to, or even exceeding, that of other reported adsorbents.

1. Introduction

Toxic metals, including "heavy metals", are hazardous elements with adverse potential for human health. These contaminants, often introduced into the environment through anthropogenic activities [1], are commonly incorporated into manufactured products and reach ecosystems through the improper disposal of materials and effluents contaminated by metal ions [2]. Due to their bioaccumulative nature and high toxicity, these elements can accumulate in plants and animals, leading to severe health effects like organ failure, reproductive malformations, and cancer [3]. Currently, the most toxic metal ions of concern are arsenic (As), cadmium (Cd), lead (Pb), copper (Cu), chromium (Cr), mercury (Hg), nickel (Ni), and zinc (Zn) [4].

Liu et al. [5] conducted a study to assess the distribution and concentration of toxic metals (Cd, Cr, Cu, Pb and Zn) in the Zijiang River (ZR), which supplies water to approximately 10 million people in Hunan province, central China. In that study, the authors found that the concentrations of these metal ions in water were below the maximum permissible limits for drinking water in China (Cd, 5 μg L^{-1}; Cr, 50 μg L^{-1}; Cu, 1 μg L^{-1}; Pb, 10 μg L^{-1}; and Zn, 1 μg L^{-1}) [5]. However, this is not the case for river sediments. The higher concentrations of Cd and Zn in the sediment surface is an indicator of moderate to severe contamination, leading the authors to recommend the implementation of effective pollution control strategies to prevent further release of metal ions into the river basin. In other study, Gundersen et al. [6] conducted seasonal monitoring of Hg(II) ion concentration in lakes and rivers across Norway and Russia, as well as in sediments and fish from these regions. While low concentration of Hg(II) was detected in the water bodies (ranging from 0.0002 to 0.042 μg L^{-1}) they also documented high levels of Hg(II) in sediments and fish throughout the region. Mercury reserves in

* Corresponding authors.
E-mail addresses: carlos.manuel@eq.uc.pt (C.M. Silva), prediger@unicamp.br (P. Prediger).

https://doi.org/10.1016/j.molliq.2025.129055
Received 8 October 2025; Received in revised form 17 November 2025; Accepted 26 November 2025
Available online 30 November 2025

sediments can be resuspended into watercourses, posing a significant risk to local populations, wildlife, and the Arctic Ocean. Despite the low concentrations in water, the bioaccumulation of these metals through the food chain emphasizes the importance of water treatment, as their transfer to living organisms could still pose significant health risks. Therefore, despite their deleterious effects on the environment and humans, the recurring presence of these pollutants in various environmental compartments highlights an inadequate disposal of contaminated materials and the inefficiency of conventional treatments [7]. To address these challenges, physicochemical treatments, oxidation/reduction processes, and biological methods have been extensively investigated in recent years for the decontamination of water resources containing rising levels of toxic metal ions [8]. Among these technologies, physicochemical treatments stand out above the others, mainly due to their reduced energy consumption and the lack of secondary pollutant generation [9].

Adsorption is a biphasic phenomenon in which compounds are transferred from a fluid phase into the porous structure of a solid, where they adhere to its internal surface. It is a widely explored method for removing metal ions from water through physicochemical processes [7]. In recent years, the application of nanomaterials as adsorbents has boosted the efficiency of this process, and several nanoadsorbents, including carbon nanotubes, metal oxide-based nanomaterials, and graphene, have already been investigated for the removal of toxic metals [10]. However, despite their high adsorption potential for metal ions, nanomaterials tend to aggregate into larger particles due to van der Waals interactions, which may penalize their adsorption capacity [11]. Additionally, their high stability in aqueous solution makes their recovery after the adsorption process expensive and economically unviable, primarily due to the requirement of additional separation steps, such as centrifugation for solid precipitation and filtration for solid removal from the medium [12]. One potential solution to these challenges is the incorporation of nanomaterials into a porous substrate [7]. This approach allows the integration of nanoadsorbents into a membrane matrix, resulting in the formation of a nanocomposite polymeric membrane. These membranes exhibit dual functionality, combining the advantages of adsorption and filtration processes [13].

In our previous work, we developed polymeric membranes of hydrolyzed polyacrylonitrile (hPAN) coated with three layers of graphene oxide (GO) and poly(4-vinyl pyridinium) (PVPI) (hereafter denoted by hPAN/PVPI$_3$/GO$_3$) using the layer-by-layer method, and these membranes were applied for the removal of Pb^{2+}, Cr^{3+}, Cu^{2+}, Ni^{2+} and Cd^{2+} from water [14]. The incorporation of PVPI and GO on the pristine hPAN modified both the surface and vicinal sub-layers of the base polymer, reduced the hydrophilicity of the material, and introduced new Lewis bases sites to the membrane, thereby enhancing its removal capacity. Even under non-optimized conditions, the hPAN/PVPI$_3$/GO$_3$ membrane demonstrated high selectivity for Cr^{3+}, Cu^{2+}, and Pb^{2+} over Ni^{2+} and Cd^{2+} ions, achieving removal efficiencies higher than 50 %, under the studied batch operating conditions. While these results highlight the membrane's promising potential, a comprehensive understanding of its adsorption behavior remains limited. Gaining insight into the fundamental mechanisms governing the interaction between the membrane and target metal ions is essential to fully exploit its performance and guide the development of next-generation materials for water purification. To address this, the present study aimed to investigate the performance of hPAN/PVPI$_3$/GO$_3$ membranes for the removal of Cr^{3+}, Cu^{2+}, and Pb^{2+} ions in batch multicomponent conditions and to elucidate the underlying adsorption mechanisms. The influence of key parameters such as solution pH and adsorbent dosage on metal uptake was evaluated, alongside the system's kinetic and equilibrium behavior. The regeneration potential of the hPAN/PVPI$_3$/GO$_3$ membrane was also evaluated over consecutive adsorption–desorption cycles. To elucidate the interaction mechanisms between the membrane and the toxic metal ions, a combination of advanced characterization techniques was employed. These included Fourier Transform Infrared Spectroscopy (FT-IR), X-ray Photoelectron Spectroscopy (XPS), Atomic Force Microscopy (AFM), Confocal Laser Scanning Microscopy (CLSM), and Scanning Electron Microscopy (SEM).

2. Experimental section

2.1. hPAN/PVPI/GO membranes preparation

A schematic diagram illustrating the steps involved in the preparation of the hPAN/PVPI/GO membrane is shown in Fig. S1. Briefly, GO was synthesized by a modified Hummers method [15], PVP was quaternized to form PVPI [16], and hPAN membranes were obtained by phase inversion and alkaline hydrolysis [17]. The final hPAN/PVPI$_3$/GO$_3$ membranes were prepared by sequential layer-by-layer deposition [18] of PVPI and GO (three alternating layers) on the hPAN membrane.

2.2. Batch adsorption assays

To study the optimal conditions for the adsorption of toxic metal ions (Cr^{3+}, Cu^{2+}, and Pb^{2+}) using the prepared membranes, the effects of pH (1.5–5.5) and membrane mass (0.01–0.10 g) were evaluated. The multicomponent contaminant solutions were synthetically formulated by dissolving appropriate amounts of analytical-grade metal salts in deionized water to obtain 20 mL of mixed-metal solutions containing all analytes simultaneously at concentrations of 20 mg L^{-1} for Cu^{2+}, 10 mg L^{-1} for Cr^{3+}, and 10 mg L^{-1} for Pb^{2+}. These concentrations were selected based on values reported in the literature [19,20]. The solution pH was adjusted using 0.1 M HCl accordingly. The membranes were cut and weighed according to the experimental design, ensuring accurate representation of the selected mass range. Experiments were carried out in triplicate on an orbital shaker (LABWIT – Shaker Incubator ZWYR-240) at constant speed of 180 rpm and room temperature. After 24 h, samples were collected, acidified, and diluted for analysis. Residual concentrations of metal ions were determined by flame atomic absorption spectroscopy (GBC, Avanta PM spectrophotometer) using a five-standards calibration curve.

The mass of metal adsorbed per unit mass of membrane at equilibrium is given by the solid concentration $q_{i,e}$ (mg g^{-1}, Eq. 1), the percentage of metal ions retained in the membrane is given by the removal efficiency $R_{e,i}$ (%, Eq. 2), and the selectivity of the membrane for ion i relative to ion j in a multicomponent system is given by the selectivity coefficient $S_{i,j}$ (Eq. 3).

$$q_{i,e} = \frac{(C_{i,0} - C_{i,f})\ V}{m} \tag{1}$$

$$R_{e,i} = 100 \times \frac{C_{i,0} - C_{i,f}}{C_{i,0}} \tag{2}$$

$$S_{i,j} = \frac{K_i}{K_j} = \frac{q_{i,e}/Ci,f}{q_{j,e}/Cj,f} \tag{3}$$

where $C_{i,0}$ and $C_{i,f}$ (mg L^{-1}) are the initial and final (equilibrium) metal concentrations in solution, respectively, V (L) is the solution volume, m (g) is the membrane mass, K_i and K_j are the distribution coefficients of the metal i or j.

2.3. Kinetic and equilibrium study

2.3.1. Kinetic study

The adsorption kinetics study of the three metals in a ternary system was carried out at pH 5.5 by fixing the solution volume (20 mL) and varying the initial mass of the hPAN/PVPI$_3$/GO$_3$ membrane from 0.01 g to 0.05 g over a time interval from 5 min to 24 h. After, the samples were collected and the residual metal ions concentration was determined by

Table 1
Kinetic models.

Models	Equation	Plot
Pseudo-first order	$\log\left(q_{i,e}-q_{i,t}\right)=\log q_{i,e}-\left(\frac{k_1}{2.303}\right)t$	$\log\left(q_{i,e}-q_{i,t}\right)$ *vs.* t
Pseudo-second order	$\frac{1}{q_{i,t}}=\frac{1}{k_2 q_{i,e}^2}+\frac{t}{q_{i,e}}$	$\frac{1}{q_{i,t}}$ *vs.* t
Intraparticle diffusion	$q_{i,t}=K_{DIF}t^{0.5}+c$	$q_{i,t}$ *vs.* $t^{0.5}$

Table 2
Isotherm models.

Models	Equation
BET	$q_{i,e}=\left(\frac{q_m b_1 C_{i,e}}{1+(b_1-b_2)C_{i,e}}\right)\left(\frac{1}{1-b_2C_{i,e}}\right)$
ASV	$q_{i,e}=\left(\frac{q_m \alpha b_2 C_{i,e}}{1-\alpha\ln(1-b_2C_{i,e})}\right)\left(\frac{1}{1-b_2C_{i,e}}\right)$
PTA	$q_{i,e}=\left(\frac{q_m b_1 C_{i,e}}{1+(b_1-b_2)C_{i,e}}\right)\left(\frac{1-\beta(b_2C_{i,e})^{n_1}}{1-b_2C_{i,e}}\right)$
AD	$q_{i,e}=\left(\frac{q_m bC_{i,e}}{1+bC_{i,e}}\right)\left(\frac{1}{(1-b_2C_{i,e})^{n_2}}\right)$

atomic flame absorption spectroscopy, on a GBC, Avanta PM spectrophotometer, using a five-standards calibration curve.

The pseudo-first order [21], the pseudo-second order [22], and the intraparticle diffusion [23] kinetic models were employed and fitted to the experimental data using the Origin Lab program. Table 1 summarizes the three kinetic models where: $q_{i,e}$ (mg g^{-1}) is the amount of metal ion adsorbed per unit mass of adsorbent at equilibrium, $q_{i,t}$ (mg g^{-1}) is the amount of adsorbed metal ions at a given time, k_1 (min^{-1}), k_2 (g m^{-1} min^{-1}) and k_{DIF} (mg g^{-1} $min^{-0.5}$) are the pseudo-first order, pseudo-second order and intraparticle diffusion adsorption rate constants, respectively, t is the adsorption time (min), and c is the y-intercept.

2.3.2. Adsorption equilibrium study

The isotherms for the three toxic metals in a ternary system were determined at pH 5.5 by fixing the solution volume (20 mL) and varying the initial mass of hPAN/$PVPI_3$/GO_3 from 0.01 to 0.13 g throughout 24 h. After equilibrium, the samples were collected and the residual metal ions concentration was determined by atomic flame absorption spectroscopy, on a GBC, Avanta PM spectrophotometer, using a five-standards calibration curve.

The BET isotherm for liquid phase adsorption [24], along with the modified BET equations due to Aguerre–Suarez–Viollaz (ASV) [25], Pantuso–Tolaba–Aguerre (PTA) [26], and Aranovich–Donohue (AD) [27,28], were selected and fitted to the experimental data using the Origin Lab program. Table 2 summarizes these equations where: $q_{i,e}$ (mg g^{-1}) is the equilibrium adsorbed phase concentration, $q_{i,m}$ (mg g^{-1}) is the monolayer adsorption capacity, $C_{i,e}$ (mg L^{-1}) is the equilibrium liquid phase concentration, b, b_1, and b_2 (L mg^{-1}) are equilibrium constants, and α, β, n_1, and n_2 are constants.

2.4. Adsorption-desorption assays

The reuse potential of the hPAN/$PVPI_3$/GO_3 membrane was evaluated through five consecutive adsorption-desorption cycles. After the multicomponent adsorption assays, the membranes loaded with the toxic metal ions were treated with aqueous solutions at either pH 1.5 or at pH 5.5. The solution pH was adjusted using 0.1 M HCl or 0.1 M NaOH accordingly. During this desorption step, the metal-loaded membranes were immersed in 20 mL of the eluting solvent in a beaker and placed in an orbital shaker (LABWIT – Shaker Incubator ZWYR-240) at 180 rpm for 24 h. After, the membranes were washed with distilled water and reused in subsequent multicomponent adsorption assays.

Table 3
Summary of the hPAN/$PVPI_3$/GO_3 membranes characterization [14].

Technique	Results
XRD	The XRD patterns of hPAN and hPAN/$PVPI_3$/GO_3 exhibited similarities, with a small sharp peak at 16.8° (100), which is attributed to the C≡N bonds, and a broad band at 23.0°, attributed to the amorphous region of the membrane.
FT-IR	The FT-IR spectrum of the hPAN/$PVPI_3$/GO_3 showed absorption bands at 3345 cm^{-1}, 2240 cm^{-1}, 1649 cm^{-1}, 1570 cm^{-1}, and 1027 cm^{-1}, which can be attributed to the stretching of the O – H, C≡N, C═O, C═C, and C – O bonds, respectively.
XPS	The presence of PVPI/GO in the membranes was confirmed by the increased in C content. The C1s high-resolution spectrum of hPAN/$PVPI_3$/GO_3 indicated peaks referring to C-sp^3/C-sp^2 (284.7 eV), C—O (286.9 eV), C═O (287.7 eV) and COOH (288.7) groups, while the N1s high-resolution spectrum showed peaks attributed to NH_2 (399.5 eV) and N-C═O/N ≡ C (400.3 eV) groups.
Morphological properties	The hPAN/$PVPI_3$/GO_3 membrane exhibited an asymmetrical, thin, and rough finger-like porous sublayer, with macrovoids and a total pore volume of 0.140×10^{-3} cm^3 g^{-1}, accompanied by a rougher surface with an average roughness (Sq) value of 240.5 nm.
Water contact angle (WCA)	A hydrophilic surface was observed on the hPAN/$PVPI_3$/GO_3 material with a WCA value of 17.7°.
Pure water flux (PWF)	The hPAN/$PVPI_3$/GO_3 membrane exhibited a PWF of 45.9 L m^{-2} h^{-1}.
Zeta potential	The incorporation of PVPI/GO on the hPAN membrane resulted in a less negative surface charge. For hPAN/$PVPI_3$/GO_3 the zeta potential was −12.8 mV at pH 6.

2.5. Post-adsorption characterization

The post-adsorption membrane was characterized using various techniques: Fourier transform infrared spectroscopy (FT-IR) analyses were performed in the range of 4000 to 400 cm^{-1} using the ATR method on a Tensor 27 Bruker FT-IR spectrometer; X-Ray photoelectron spectroscopy (XPS) was conducted using a ScientaOmicron ESCA+ spectrometer with a hemispherical analyzer (EAC2000), monochromatic Al Kα radiation ($h\nu = 1486.6$ eV) as the excitation source, and an operating pressure of 10^{-9} Pa. A charge neutralizer (CN10) was used to mitigate surface charging effects. Energy steps of 0.1 eV and 0.05 eV were used for the survey and high-resolution spectra, respectively, within an energy range between 0 and 1200 eV. Data analysis was performed using the Casa XPS software; Confocal laser scanning microscopy (CLSM) was performed on dried membrane samples using a Keyence LSC VK-X200 equipment with a 10× and 150× confocal lens at a wavelength of 408 nm; Scanning electron microscopy (SEM) was carried out on a Tescan equipment Vega 3 SEM at 30 kV with a scan spacing of 180 mm; Atomic force microscopy (AFM) was carried out on a JPK NanoWizard4 equipment, with a resonance frequency of 150 kHz and a constant nominal force of 0.7 N m^{-1}, with a 512 × 512 pixels resolution. Image processing and statistical calculations were carried out using the Gwyddion software.

3. Results and discussion

3.1. Preparation and characterization of hPAN/$PVPI_3$/GO_3 membranes

The preparation of a membrane, based on hPAN coated with alternating layers of PVPI and GO, was designed with the aim of developing materials with potential applications in adsorption processes of water and wastewater. PAN, a low-cost synthetic polymer containing nitrile groups, has the capacity to interact with chemical pollutants through

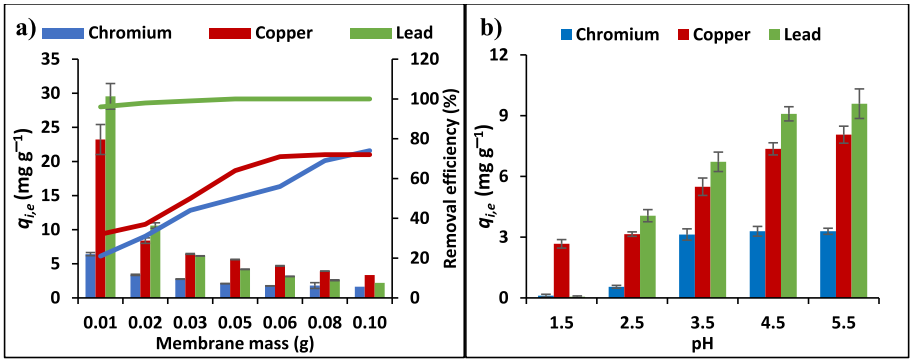

Fig. 1. a) Membrane mass variation from 0.01 g to 0.10 g at initial pH 5.5. **b)** Initial pH variation from 1.5 to 5.5 for a membrane mass of 0.02 g. Fixed conditions: membranes with 3 layers of adsorbent on the pristine membrane (hPAN/PVPI$_3$/GO$_3$), 20 mL of solution with 10 mg L^{-1} Cr^{3+} and Pb^{2+}, and 20 mg L^{-1} of Cu^{2+}, room temperature, and contact time of 24 h. Bars represent adsorbent phase concentration; curves represent removal efficiency.

electron-rich and electron-deficient sites [29]. However, it demonstrates limitations in terms of pore size, flux, and fouling resistance [30]. The incorporation of GO, a nanoadsorbent derived from partially oxidized graphite, improves chemical and morphological properties, enhancing selectivity, hydrophilicity, and water permeability. However, electrostatic repulsion between hPAN and GO requires a cationic component to ensure layer adhesion [31]. In this regard, PVPI was employed to promote electrostatic attraction, provide bactericidal activity, and enable cation–π interactions with aromatic pollutants, thereby enhancing the membrane's adsorptive performance.

In Table 3 a summary of the characterization results of the prepared hPAN/PVPI$_3$/GO$_3$ membranes is presented [14].

The removal of multiple toxic metals from aqueous solution was previously evaluated [14] to assess the effect of PVPI/GO layers on the adsorption capacity of pristine hPAN. The results showed that the incorporation of PVPI/GO on the polymeric matrix resulted in morphological and physicochemical modifications of the pristine membrane, thereby enhancing the adsorption ability of hPAN. Among the toxic metals evaluated, the new membranes exhibited superior performance compared to the pristine polymer for Cr^{3+}, Cu^{2+}, and Pb^{2+} ions over Cd^{2+} and Ni^{2+} ions. Notably, the hPAN/PVPI₃/GO₃ membrane, incorporating three alternating PVPI/GO layers, showed the highest adsorption potential among the prepared membranes. Therefore, Cr^{3+}, Cu^{2+}, and Pb^{2+} were selected for further investigation of the adsorptive potential and interactions in hPAN/PVPI3/GO3 membranes.

3.2. Adsorption of toxic metals in multicomponent systems

3.2.1. Influence of hPAN/PVPI$_3$/GO$_3$ mass

The adsorption performance of the hPAN/PVPI$_3$/GO$_3$ membranes for a ternary system containing Cr^{3+}, Cu^{2+}, and Pb^{2+} was evaluated as a function of the mass of the material, varying from 0.01 g to 0.10 g, with a constant solution volume of 20 mL. The evolution of the adsorption potential of the membrane for the three metal ions is illustrated in Fig. 1a. The adsorption profile exhibited by the membrane in response to all the ions evaluated was found to be broadly similar. The adsorption performance expressed in $q_{i,e}$ (equilibrium concentration in the hPAN/PVPI$_3$/GO$_3$ membrane) gradually decreased as the membrane mass increased, accompanied by a corresponding increase in the percentage of contaminant removal.

Upon an initial membrane mass of 0.01 g, it was observed that higher $q_{i,e}$ and lower $R_{e,i}$ were obtained for the metal ions in the ternary system (Fig. 1a), with values of 6.42 mg g^{-1} (21 %), 23.2 mg g^{-1} (32 %) and 29.6 mg g^{-1} (96 %) for Cr^{3+}, Cu^{2+} and Pb^{2+}, respectively. Conversely, for a mass of 0.1 g, the values were reversed for both $q_{i,e}$ and $R_{e,i}$. The values were 1.65 mg g^{-1} (73 %), 3.35 mg g^{-1} (72 %) and 2.21 mg g^{-1} (100 %) for Cr^{3+}, Cu^{2+} and Pb^{2+}, respectively.

In all assays, increasing the mass of adsorbent resulted in an increase in the number of active sites available for adsorption. Given that the volume of the solution and the initial concentration of adsorbates were fixed in the tests, it was observed that an increase in the mass of adsorbent led to a reduction in the occupation of the active centers of hPAN/PVPI$_3$/GO$_3$, resulting in a decrease in $q_{i,e}$. Concurrently, an increase in the relative amount of adsorbate removed from the aqueous medium in relation to the total available was noted, leading to an increase of $R_{e,i}$. Similar results were reported by Pang et al. [32], who utilized red mud modified with amorphous MnO_2 (MRM) to remove cadmium from aqueous solution. The authors observed that increasing the adsorbent dosage in the medium from 0.2 to 12 g L^{-1} led to a non-proportional increase in the removal percentage and a decrease in the solid concentration. In our essays, in addition to the variations in $q_{i,e}$ and $R_{e,i}$ observed for each individual metal ion, differences were also noted among the three metal ions, reflecting selective adsorption behavior. Both phenomena can be explained by the non-linearity of the adsorption equilibrium and/or to the competition for the adsorbent's sites by the different ions present in the medium. The non-linearity of the adsorption process can be explained by the heterogeneity of the membrane surface, competition for the active sites of the adsorbent by the different adsorbates, and/or range of operating conditions [33,34]. Concerning the competition for active sites, one adsorbate may exhibit a higher affinity for the adsorbent, lizmiting the adsorption of the other ions and affecting the overall removal efficiency [35].

3.2.2. Influence of initial pH

Since the pH of the medium affects the protonation of chemical functional groups in the adsorbent and the ionic charge of the adsorbate, it is one of the most important parameters in adsorption processes [36]. To assess the effect of pH on the adsorption of metal ions in a multicomponent system by the membrane, hPAN/PVPI$_3$/GO$_3$ was used in adsorption experiments by varying the initial pH of the solution from 1.5 to 5.5 (Fig. 1b). The selection of the pH in the acidic range was based on the fact that metal ions precipitate at pH values above 6, which is associated with the formation of metal oxides and hydroxides [37].

For Cu^{2+} and Pb^{2+}, the membrane showed a similar adsorption profile (Fig. 1b). There was a gradual increase of the hPAN/PVPI$_3$/GO$_3$ loading with the increasing pH of the medium. Cr^{3+} exhibited a similar pattern, with an initial increase up to pH 3.5, after which the system's adsorption remained constant. The adsorption values for Cu^{2+} were 2.67 mg g^{-1}, 3.15 mg g^{-1}, 5.49 mg g^{-1}, 7.36 mg g^{-1}, and 8.06 mg g^{-1}; and for Pb^{2+} were 0.06 mg g^{-1}, 4.06 mg g^{-1}, 6.72 mg g^{-1}, 9.09 mg g^{-1}, and 9.59 mg g^{-1}; for Cr^{3+} were 0.11 mg g^{-1}, 0.55 mg g^{-1}, 3.13 mg g^{-1}, 3.29 mg g^{-1}, and 3.30 mg g^{-1} at pH 1.5, 2.5, 3.5, 4.5, and 5.5, respectively.

These trends can be elucidated by the influence of pH both on the membrane surface and on the chemical speciation of the metal cations in solution. Increasing the pH promotes the deprotonation of the carboxylic and hydroxyl groups present in GO and hPAN (Table 3), which

contributes to an increase of the negative charge of the hPAN/PVPI$_3$/GO$_3$ membrane surface, thereby facilitating the adsorption of cationic species [38]. Regarding the metal cations, within the evaluated pH range, the predominant species for Pb and Cu are Pb^{2+} and Cu^{2+} [39,40], while for Cr the major species is Cr^{3+} at pH 1.5–3.5 and Cr $(OH)^{2+}$ between pH 3.5 and 5.5 [41]. Under highly acidic conditions, competition between H^+ ions and metal cations for the active sites on the membrane surface limits adsorption. As the pH increases, the progressive deprotonation of the functional groups of the adsorbent, along with the formation of hydroxylated chromium species, enhances electrostatic interactions and promotes the formation of coordination complexes between the metal cations and the oxygenated groups on the membrane surface [42].

Similar results were observed by Hosseinkhani et al. [43], who studied the influence of the pH of the medium on the adsorption of metal cations (Cd^{2+} and Pb^{2+}) by graphene oxide/ZnO nanocomposites. According to the authors [43], an increase in pH resulted in an increase in the surface charge of the GO, meaning that the electrostatic interactions between the material's nanosheets and the heavy metal ions became stronger, resulting in improved sorption of Cd^{2+} and Pb^{2+} ions. In addition, the authors [43] attributed the low adsorption of Cd^{2+} and Pb^{2+} in very acidic conditions to competition between the metal cations and hydrogen cations on the sites of the surface nanoadsorbent.

Based on these findings, pH 5.5 was selected as the ideal condition for conducting the membrane/toxic metal adsorption studies.

3.2.3. Selectivity analysis

In multicomponent adsorption systems, selectivity is a critical factor that determines the applicability of adsorbent materials to real effluents. The results obtained for Cr^{3+}, Cu^{2+}, and Pb^{2+} uptake revealed that, besides the variations in $q_{i,e}$ observed for each ion under different operational conditions (membrane mass and pH), there were also clear differences among the three metals, evidencing selective adsorption by the hPAN/PVPI₃/GO₃ membranes.

In summary, the hPAN/PVPI$_3$/GO$_3$ membrane showed experimental maximum adsorption capacities of 6.42 mg g^{-1}, 23.2 mg g^{-1}, and 29.6 mg g^{-1} for Cr^{3+}, Cu^{2+}, and Pb^{2+}, respectively, when using a membrane mass of 0.01 g at 298 K and pH 5.5, with initial concentrations of 10 mg L^{-1} of Cr^{3+} and Pb^{2+} and 20 mg L^{-1} of Cu^{2+}. Concerning the calculated selectivities (relative to Cr^{3+}), the values obtained were 1.00, 2.03, and 81.2 for Cr^{3+}, Cu^{2+}, and Pb^{2+}, respectively (Table S1). The membrane thus showed markedly higher selectivity for Pb^{2+}, followed by Cu^{2+} and Cr^{3+}.

This preferential affinity toward Pb^{2+} can be attributed to physicochemical characteristics of the ions, such as ionic radius, hydration energy, and their stronger tendency to interact with the hPAN/PVPI$_3$/GO$_3$ membrane [14]. Pb^{2+} has the largest Pauling ionic radius (1.18 Å) [44] and the lowest hydration enthalpy (−1481 kJ mol^{-1}) [45], which favors dehydration and direct interaction with the electron-rich functional groups of GO, PVPI, and hPAN. Conversely, Cr^{3+}, with the smallest Pauling ionic radius (0.62 Å) [44] and the highest hydration enthalpy (−4560 kJ mol^{-1}) [45], tends to retain its hydration shell more strongly, inhibiting effective coordination with the membrane surface. Cu^{2+} presents intermediate properties (Pauling ionic radius 0.73 Å [44] and hydration enthalpy −2100 kJ mol^{-1} [45]), which is consistent with its intermediate selectivity compared to Pb^{2+} and Cr^{3+}.

Furthermore, the selective adsorption observed can be attributed by the non-linearity of adsorption equilibrium in multicomponent systems, as well as competition among the cations for the available active sites [35]. In such systems, ions with higher affinity dominate the adsorption process, reducing the uptake of less competitive species. This explains both the divergences in adsorption capacity among different metals and the intra-ion variations observed for each individual species under varying experimental conditions.

These findings align with reports in the literature, where multimetal adsorption studies frequently highlight the preferential removal of specific ions depending on adsorbent surface chemistry, ion characteristics, and experimental conditions [44,46,47].

Table 4
Kinetic parameters for the adsorption of the metal ions on hPAN/PVPI$_3$/GO$_3$. Experimental conditions: membranes with 3 layers of adsorbent on the pristine membrane (hPAN/PVPI$_3$/GO$_3$), 20 mL of solution with 10 mg L^{-1} Cr^{3+} and Pb^{2+}, and 20 mg L^{-1} of Cu^{2+}, room temperature, pH 5.5, and contact time from 0 to 24 h.

		Cr^{3+}			
		0.01 g	**0.02 g**	**0.03 g**	**0.05 g**
Experimental $q_{i,e}$ (mg g^{-1})		7.82	3.32	2.56	2.09
Pseudo-first order	k_1 (min^{-1})	1.20E-03	2.30E-03	2.30E-03	2.80E-03
	$q_{i,e}$ (mg g^{-1})	4.10	1.12	1.40	1.26
	R^2	0.88	0.86	0.94	0.91
Pseudo-second order	k_2 (g mg^{-1} min^{-1})	**1.70E-03**	**1.13E-02**	**6.70E-03**	**7.40E-03**
	$q_{i,e}$ (mg g^{-1})	**6.68**	**3.23**	**2.58**	**2.09**
	R^2	**0.97**	**0.99**	**0.99**	**0.99**
Intraparticle diffusion	k_{DIF} (mg g^{-1} $min^{-0,5}$)	0.13	0.04	0.05	0.04
	R^2	0.91	0.78	0.90	0.91
		Cu^{2+}			
		0.01 g	**0.02 g**	**0.03 g**	**0.05 g**
Experimental $q_{i,e}$ (mg g^{-1})		24.75	8.24	6.42	5.70
Pseudo-first order	k_1 (min^{-1})	2.10E-03	3.00E-03	1.20E-03	3.00E-03
	$q_{i,e}$ (mg g^{-1})	9.75	2.31	2.72	2.98
	R^2	0.94	0.87	0.78	0.96
Pseudo-second order	k_2 (g mg^{-1} min^{-1})	**1.00E-03**	**6.50E-03**	**3.50E-03**	**3.60E-03**
	$q_{i,e}$ (mg g^{-1})	**24.81**	**8.28**	**6.20**	**5.69**
	R^2	**0.99**	**0.99**	**0.99**	**0.99**
Intraparticle diffusion	k_{DIF} (mg g^{-1} $min^{-0,5}$)	0.29	0.09	0.09	0.09
	R^2	0.90	0.80	0.92	0.94
		Pb^{2+}			
		0.01 g	**0.02 g**	**0.03 g**	**0.05 g**
Experimental $q_{i,e}$ (mg g^{-1})		31.4	9.87	5.68	3.99
Pseudo-first order	k_1 (min^{-1})	3.40E-03	3.70E-03	5.50E-03	1.17E-02
	$q_{i,e}$ (mg g^{-1})	21.44	4.29	1.41	1.01
	R^2	0.98	0.93	0.86	0.91
Pseudo-second order	k_2 (g mg^{-1} min^{-1})	**4.00E-04**	**5.50E-03**	**1.54E-02**	**4.64E-02**
	$q_{i,e}$ (mg g^{-1})	**32.7**	**9.98**	**5.73**	**3.97**
	R^2	**0.99**	**0.99**	**0.99**	**0.99**
Intraparticle diffusion	k_{DIF} (mg g^{-1} $min^{-0,5}$)	0.74	0.17	0.08	0.03
	R^2	0.86	0.65	0.62	0.46

3.3. Kinetics and equilibrium study

3.3.1. Adsorption kinetics

Adsorption kinetics refers to the rate at which solutes adsorb onto the solid surface over time [48], which depends on film diffusion, intraparticle diffusion, and the local adsorption rate [48,49]. Therefore, the kinetic parameters involved in the uptake of Cr^{3+}, Cu^{2+}, and Pb^{2+} by hPAN/PVPI$_3$/GO$_3$ membranes were investigated by fitting pseudo-first order [21], pseudo-second order [22], and intraparticle diffusion [23] kinetic models to the experimental data. The adjusted parameters from this analysis are listed in Table 4, with the best-fitting model determined based on a high coefficient of determination (R^2) value and a low variance between the calculated and experimental $q_{i,e}$ (value)

The results showed that the pseudo-second order model was consistent with the experimental data for the three metal ions, with R^2 above 0.98 for Cr^{3+}, Cu^{2+}, and Pb^{2+} (Table 4). Fig. S2 summarizes the pseudo second-order model fits to the experimental data. This model

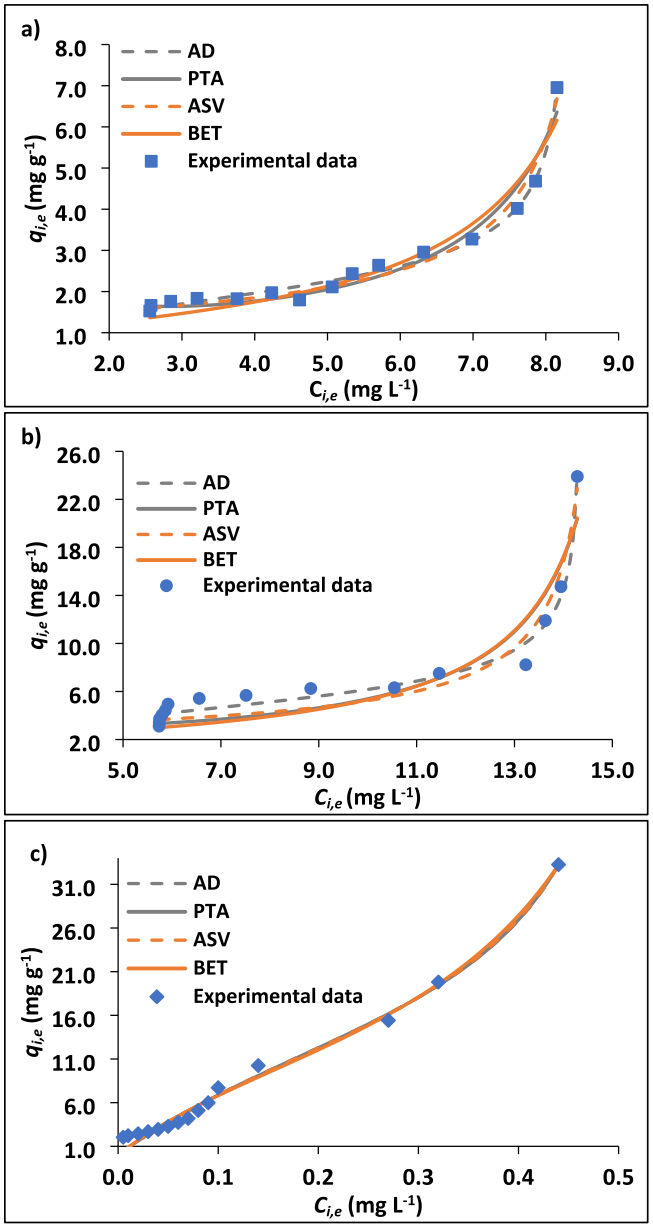

Fig. 2. BET, ASV, PTA, and AD adsorption isotherm models for **a)** Cr^{3+}, **b)** Cu^{2+}, and **c)** Pb^{2+} on hPAN/$PVPI_3$/GO_3 in a ternary system. Experimental conditions: membranes with 3 layers of adsorbent on the pristine membrane (hPAN/$PVPI_3$/GO_3), membrane mass from 0.01 g to 0.1 g, 20 mL of solution with 10 mg L^{-1} of Cr^{3+} and Pb^{2+}, and 20 mg L^{-1} of Cu^{2+}, room temperature, pH 5.5, and contact time of 24 h.

states that the rate of occupation of the active sites on the hPAN/$PVPI_3$/GO_3 membrane by the metal ions is proportional to the square of the number of unoccupied centers in the solid [50].

Similarly, Silva et al. [51] investigated the simultaneous adsorption of multiple metals from aqueous solutions, including Al(III), Ba(II), Pb (II), Cu(II), Cr(III), Fe(II), Mn(II), and Zn(II), using a bioadsorbent based on banana peel flour (BPF) and a synthetic adsorbent consisting of magnetite encapsulated with chitosan (MEC). The authors reported that the pseudo-second-order model best described the adsorption kinetics for all metals on both adsorbents. Furthermore, Al-Amrani et al. [52], in a state-of-the-art review on the adsorptive removal of heavy metals from wastewater using emerging nanostructured materials, summarized that the adsorption kinetics of heavy metals in various adsorbents, such as layered double/triple hydroxides (LDHs/LTHs), carbon nanotubes

Table 5
Equilibrium parameters of Cr^{3+}, Cu^{2+}, and Pb^{2+} adsorption on the hPAN/$PVPI_3$/GO_3 membrane. Experimental conditions: membranes with 3 layers of adsorbent on the pristine membrane (hPAN/$PVPI_3$/GO_3), membrane mass from 0.01 g to 0.1 g, 20 mL of solution with 10 mg L^{-1} of Cr^{3+} and Pb^{2+}, and 20 mg L^{-1} of Cu^{2+}, room temperature, pH 5.5, and contact time of 24 h.

Isotherm/metal cation	Cr^{3+}	Cu^{2+}	Pb^{2+}
BET			
q_m (mg g^{-1})	1.07	1.98	12.33
b_1 (L mg^{-1})	4.93	3.00	7.49
b_2 (L mg^{-1})	0.10	0.06	1.51
R^2	0.93	0.86	0.99
ASV			
q_m (mg g^{-1})	1.34	2.83	18.14
b_2 (L mg^{-1})	0.11	0.07	1.76
α	6210	86,900	2.71
R^2	0.98	0.95	0.99
PTA			
q_m (mg g^{-1})	1.26	8.21	13.51
b_1 (L mg^{-1})	1.08	1.07	6.34
b_2 (L mg^{-1})	1.18	1.13	1.75
β	1.70	1.23	0.60
n_1	0.00	0.00	1.64
R^2	0.94	0.85	0.99
AD			
q_m (mg g^{-1})	2.05	6.03	22.90
b (L mg^{-1})	0.83	0.24	3.72
b_2 (L mg^{-1})	0.12	0.07	1.88
n_2	0.33	0.31	0.48
R^2	**0.99**	**0.97**	0.99

(CNTs), graphene-based materials, MXenes, metal-organic frameworks (MOFs), and zeolitic imidazolate frameworks (ZIFs), generally followed the pseudo-second-order model.

3.3.2. *Adsorption isotherms*

Adsorption isotherms represent the relationship between the adsorbate concentration in the solid ($q_{i,e}$) and the concentration of adsorbate in the liquid phase ($C_{i,e}$) under equilibrium. It is a fundamental tool for understanding how adsorbates distribute between the fluid and solid phases when equilibrium is reached and may unveil the mechanisms of adsorbent/adsorbate interaction [53]. The equilibrium experiments for the three metal ions in the ternary system were carried out at pH 5.5 during 24 h and room temperature, by varying the initial mass of the hPAN/$PVPI_3$/GO_3 from 0.01 to 0.13 g (Fig. 2) while keeping the solution volume and the initial ions concentrations constant.

Fig. 2 indicated that the competitive adsorption of the different metal cations from solution with the hPAN/$PVPI_3$/GO_3 membrane was an unfavorable process, and the simple Langmuir or Freundlich models could not be applied. This suggests that the process integrated concepts from different adsorption theories by considering the complexity of multicomponent systems. Consequently, the findings were more effectively modeled using approaches that allow the examination of multiple sorption mechanisms [54], including the BET isotherm [25] and the modified BET equations of Aguerre–Suarez–Viollaz (ASV) [26], Pantuso–Tolaba–Aguerre (PTA) [27], and Aranovich–Donohue (AD) [28,29] (Fig. 2). The corresponding calculated parameters are presented in Table 5. The criterion for determining the best model was the highest R^2 (value)

Commonly used to represent data from Type II isotherms, the BET equation for the liquid phase and its modifications are based on the concept of multilayer adsorption, the first from a polynomial function and the others from power law and transcendental functions. For the Cr^{3+} and Cu^{2+} isotherms, the AD model was the one that best fitted the

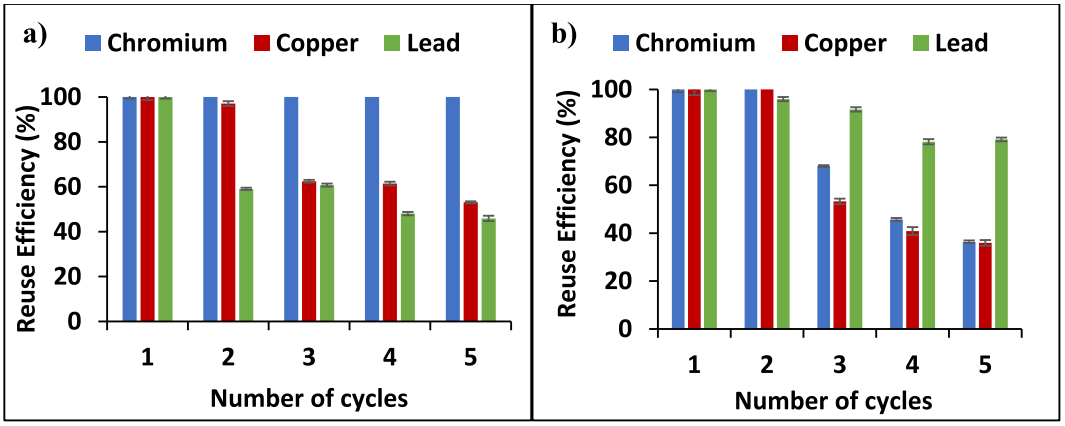

Fig. 3. Experimental conditions for metal adsorption assays: membranes with 3 layers of adsorbent on the pristine membrane (hPAN/$PVPI_3$/GO_3), membrane mass of 0.02 g, 20 mL of solution with 10 mg L^{-1} of Cr^{3+} and Pb^{2+}, and 20 mg L^{-1} of Cu^{2+}, room temperature, pH 5.5, and contact time of 24 h. Experimental conditions for metal desorption assays: membrane mass of 0.02 g, 20 mL of eluent solvent, room temperature, and contact time of 24 h. For the desorption tests the eluent solvent was **a)** pH 1.5 and **b)** pH 5.5.

experimental data, with R^2 values of 0.99 and 0.97, respectively (Table 5). For the Pb^{2+} equilibrium, the R^2 value of the four isotherms is 0.99, which suggests that all models fit the experimental data equally well (Table 5).

The parameters calculated for Cr^{3+}, Cu^{2+}, and Pb^{2+} (Table 5) indicated that the difference in the magnitude of the equilibrium constants for the first layer (b_1 or b) and the subsequent layers (b_2), consistently higher for the first and lower for the upper layers, suggests that the adsorbent/adsorbate interaction energy is stronger in the first layer than in the successive ones [55]. Accordingly, as postulated by the BET model, it can be suggested that the Cr^{3+}, Cu^{2+}, and Pb^{2+} removal mechanism in hPAN/$PVPI_3$/GO_3 encompasses process that goes beyond trivial adsorption.

Brião et al. [56] obtained analogous results in their study of the adsorption of dysprosium on expanded vermiculite. With an isotherm with an inflection point, the BET model exhibited an optimal fit of the experimental data, indicating the formation of a first homogeneous layer followed by the subsequent surface precipitation of the metal on this layer. Raji et al. [57] reached analogous conclusions upon analyzing and synthesizing information on the mechanisms of toxic metal adsorption on different adsorbents. As indicated by the findings of the study, the process of metal adsorption on activated carbon is a multifaceted phenomenon that encompasses a variety of mechanisms. These mechanisms include physical adsorption, electrostatic adsorption, ion exchange, reduction, complexation, and surface precipitation [57,58]. For biochar, three main processes are involved in the removal of toxic metals: (i) the initial deposition of the contaminant on the surface of the adsorbent, (ii) the diffusion of the adsorbate through the pores of the biochar, and (iii) the subsequent formation of layers on the surface of the adsorbent due to the surface precipitation of the adsorbate [57,59].

Additionally, in a research study, Bullen et al. [60] investigated the mechanisms of arsenic removal in TiO_2/Fe_2O_3 composites in groundwater using spectrophotometric analyses. Based on extended X-ray absorption fine structure (EXAFS) spectroscopy, FT-IR spectroscopy, and zeta potential analyses, the authors confirmed the formation of surface complexes, speciation and As(III) precipitation onto TiO_2/Fe_2O_3 composites.

Accordingly, it can be posited that the adsorption of metal cations on the hPAN/$PVPI_3$/GO_3 membrane is predominantly driven by complexation mechanisms that leads to the formation of a monolayer of ions. Conversely, surface precipitation is responsible for the formation of multilayers, wherein precipitated layers cover the first adsorbed layer [13,61]. The findings indicate that, within the context of competitive adsorption in multi-metal systems, selective sorption can occur depending on the metal affinity to the membrane surface or the precipitate surface.

3.4. *Reuse of the membrane*

The ability of new adsorbents to be reused in consecutive adsorption tests without loss of efficiency is a fundamental parameter for evaluating their functionality and practical applicability [62]. Recyclability tests were conducted using the hPAN/$PVPI_3$/GO_3 membrane, which was subjected to acidic (pH 1.5) and approximately neutral (pH 5.5) solutions during the desorption stage. These tests were conducted over five consecutive cycles, and the overall results of the adsorption of Cr^{3+}, Cu^{2+}, and Pb^{2+} in a multicomponent system, using the different eluent solutions, are presented in Fig. 3.

The hPAN/$PVPI_3$/GO_3 membrane maintained a Cr^{3+} adsorption efficiency of 100 % after five reuse cycles when an acidic solution was used as the eluent (Fig. 3a). In the case of Cu^{2+}, the membrane exhibited approximately 100 % efficiency up to the second reuse cycle, though a gradual decline was observed, with efficiency decreasing to 53 % and 34 % after five reuse cycles when acidic and neutral eluents were used, respectively (Fig. 3a-b). For Pb^{2+} removal, the membrane's performance remained high, with only 21 % decrease efficiency after five reuse cycles with *ca.* neutral eluent (Fig. 3b).

In summary, the membrane maintained high adsorption efficiency for Cr^{3+} and Pb^{2+} over five consecutive cycles when using acidic and neutral eluents, respectively. However, regardless of the eluent employed, a low adsorption efficiency was observed for Cu^{2+}. This behavior may be associated with the membrane and Cu^{2+} interactions. Post-adsorption characterizations revealed that Cu^{2+} was partially reduced to Cu^{+} during the adsorption process. The Cu^{+} ion, compared to cations analyzed, possesses the largest Pauling ionic radius (1.40 Å) [44] and the lowest enthalpy hydration (−593 kJ mol^{-1}) [45]. These properties favor the retention of the metal at the active sites of the membrane, as the larger ionic size and lower degree of hydration enhance the formation of strong interactions between the adsorbate and the adsorbent. Consequently, these stronger interactions inhibit metal desorption, explaining the low adsorption efficiency of membrane in more than two cycles for Cu^{2+} in both eluents tested [63]. Similar conclusions were reported by Xia et al. [64]. According to the authors, the strong adsorption of ionic species on graphene-based materials can inhibit the desorption of metal ions from the solid surface, especially when conventional eluents such as acidic or basic media are used. This effect ultimately leads to low reusability efficiency of these materials for metallic ions.

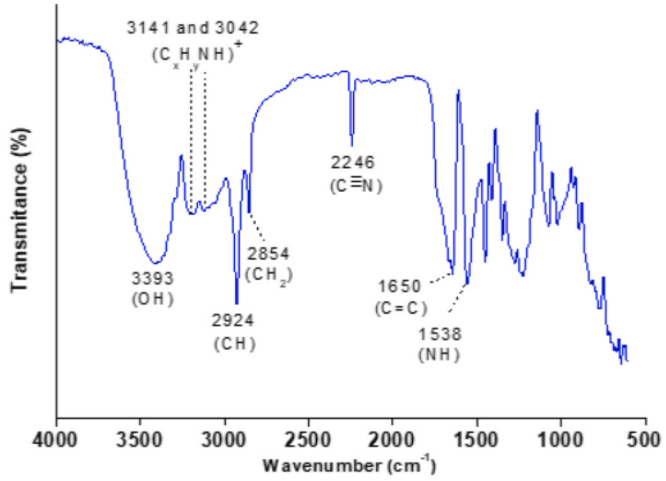

Fig. 4. FT-IR spectrum of hPAN/$PVPI_3$/GO_3 loaded with Cr^{3+}/Cu^{2+}/ Pb^{2+} ions.

3.5. Adsorption mechanism based on FT-IR, XPS, AFM, CLSM and SEM analyses

3.5.1. FT-IR, XPS, AFM, CLSM and SEM post-adsorption analyses

To elucidate the interactions of the toxic metals with the hPAN/$PVPI_3$/GO_3 membrane, a series of post-adsorption analyses were conducted, including FT-IR, XPS, CLSM, SEM, and AFM. The FT-IR analysis was used to examine the functional groups at hPAN/$PVPI_3$/GO_3 surface and identify any changes that occurred during the toxic metal adsorption (Fig. 4), demonstrating the formation of membrane/metal ions complexes. The FT-IR spectrum of the pristine hPAN/$PVPI_3$/GO_3 membrane (Table 3) exhibited characteristic bands indicative of the functional groups of the materials' composition. A broad band in the region of 3436 cm^{-1}, attributed to OH stretching, a sharp band at 2240 cm^{-1}, associated with nitrile groups (C≡N), and bands centered at 1649 cm^{-1}, 1570 cm^{-1} and 1027 cm^{-1}, assigned to C═C stretching, NH bending and C-O-C stretching vibrations, respectively [14], were observed in the spectrum of the pristine membrane. After the adsorption process, shifts in some bands and the appearance of new ones were detected in the FTIR spectrum, suggesting interactions between the adsorbent and the adsorbate. The bands corresponding to the OH (3436 cm^{-1}) and NH (1570 cm^{-1}) stretching vibrations in the hPAN/$PVPI_3$/GO_3 spectrum (Table 3) exhibited blue-shifts to 3393 cm^{-1} and 1547 cm^{-1}, respectively, in the spectrum of the loaded membrane (Fig. 4). This suggests the formation of interactions between the metal cations and the oxygen- and nitrogen-containing functional groups within the membrane structure [65,66]. Furthermore, the emergence of bands at 3141/3042 cm^{-1}, 2924 cm^{-1}, and 2854 cm^{-1}, attributed to the NH stretching vibrational modes of pyridinium, symmetric and asymmetric CH stretching of aliphatic acids, and symmetric CH_2 stretching [65], respectively, suggests that the adsorbent/adsorbate interactions lead to electron delocalization within the conjugated structure [67].

Furthermore, to elucidate the established adsorbent/adsorbate interactions, XPS analysis was performed on the hPAN/$PVPI_3$/GO_3 membrane after adsorption (Fig. 5). The XPS survey spectrum confirmed the presence of the metal cations on the loaded membrane, with relative atomic contents of 0.8 %, 0.9 %, and 0.2 % for Cr^{3+}, Cu^{2+}, and Pb^{2+}, respectively (Fig. 5a). High-resolution XPS spectra of the individual metals provide further insights into the nature of the adsorbent/adsorbate interactions and metal oxidation states (Fig. 5b-d). In the case of Cr (Fig. 5b), the spectrum displayed the presence of two peaks, with two components in which peak. The components at binding energies of 586.1 eV (Cr $2p_{1/2}$) and 576.4 eV (Cr $2p_{3/2}$) correspond to Cr^{3+} in Cr_2O_3 (30.2 %), while the peaks at 587.4 eV (Cr $2p_{1/2}$) and 577.5 eV (Cr $2p_{3/2}$) are attributed to Cr^{3+} in $Cr(OH)_3$/Cr(III)-acetate (69.8 %) [68,69]. The presence of Cr—O bonds indicates interactions between Cr^{3+} and

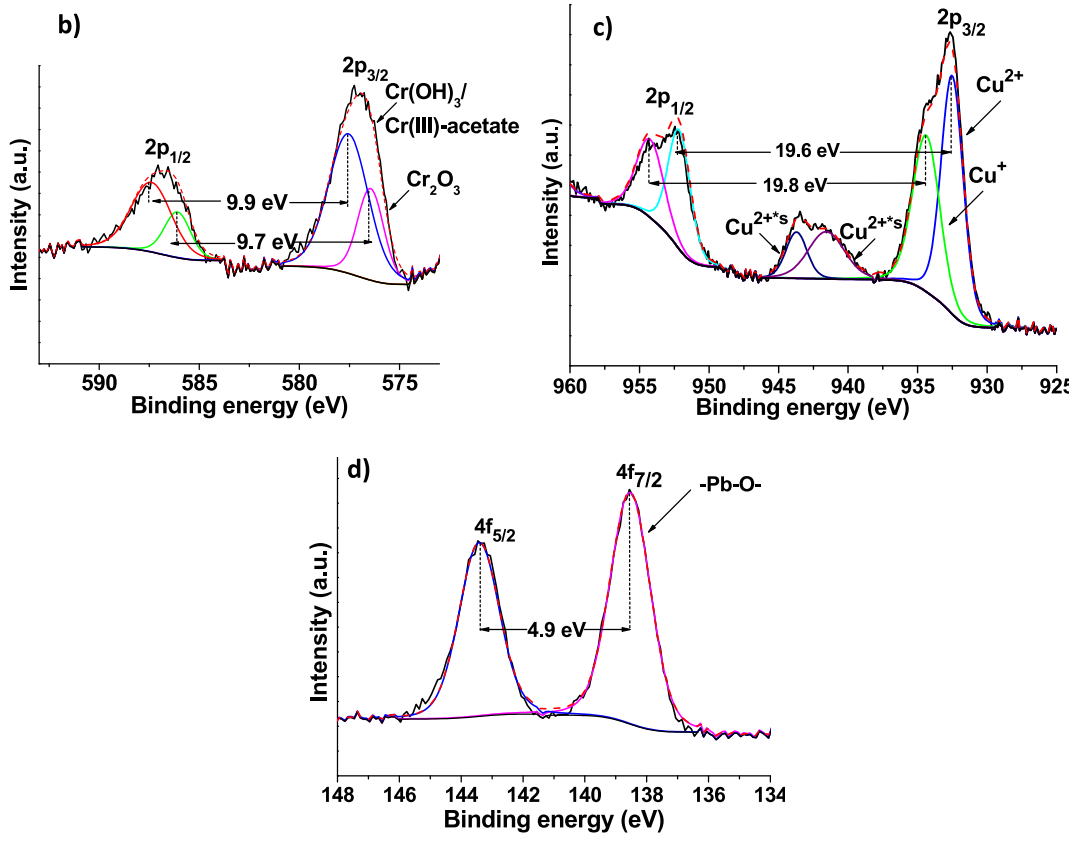

Fig. 5. a) XPS data obtained from the survey spectrum of the loaded membrane. High-resolution XPS spectra of the loaded membrane for **b)** Cr, **c)** Cu, and **d)** Pb.

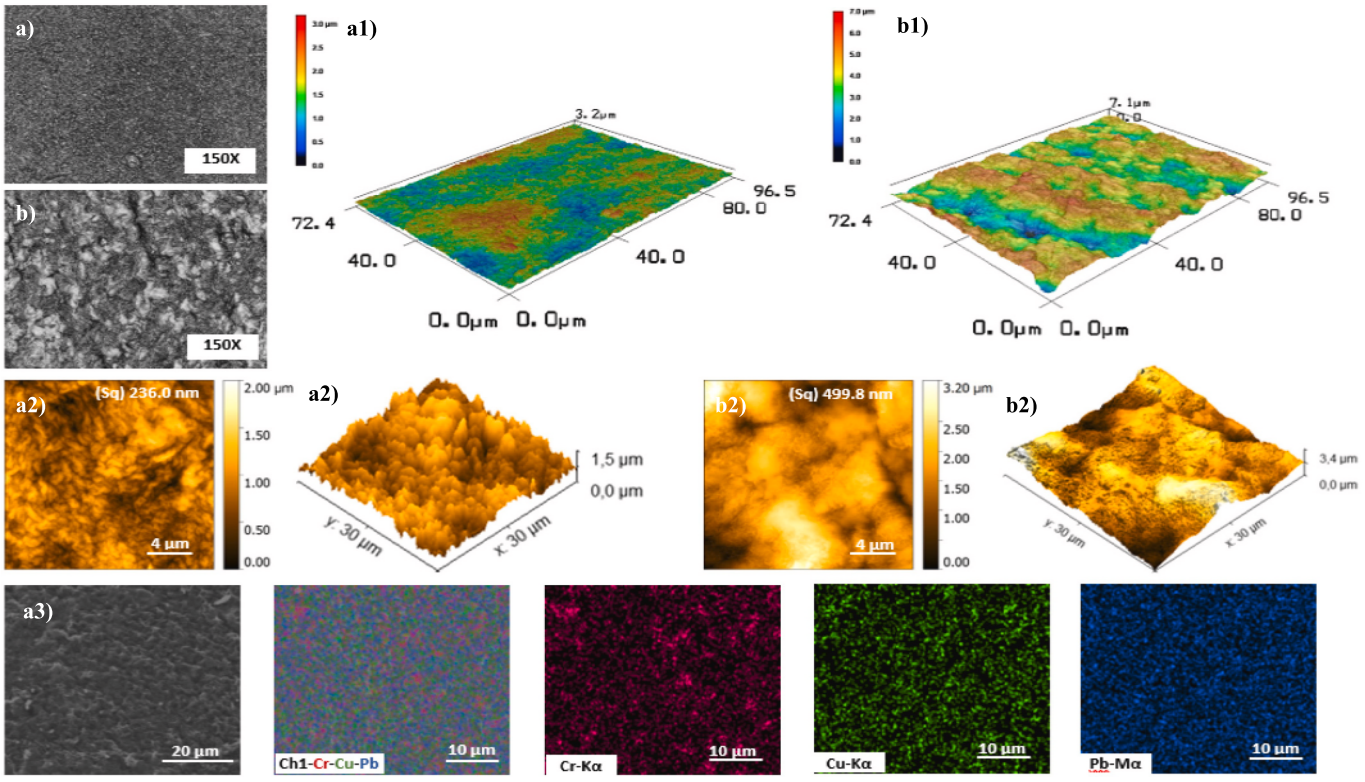

Fig. 6. Confocal images of membrane surfaces and 3D membranes surfaces for **a – a1)** hPAN/PVPI$_3$/GO$_3$, and **b – b1)** hPAN/PVPI$_3$/GO$_3$ loaded with Cr^{3+}/Cu^{2+}/Pb^{2+}. AFM images of **a2)** hPAN/PVPI$_3$/GO$_3$, and **b2)** hPAN/PVPI$_3$/GO$_3$ loaded with Cr^{3+}/Cu^{2+}/Pb^{2+}. **a3)** SEM-EDS mapping images of the surface of hPAN/PVPI$_3$/GO$_3$ loaded with Cr^{3+}/Cu^{2+}/Pb^{2+}.

oxygenated functional groups of hPAN/PVPI$_3$/GO$_3$. Furthermore, the substantial energy separation between the components of both species (9.7 eV and 9.9 eV) further supports these findings [70].

The high-resolution XPS spectrum of Cu (Fig. 5c) revealed the presence of four characteristic peaks, including two main doublets and two associated satellite peaks. The peaks at binding energies of 952.1 eV (Cu $2p_{1/2}$) and 932.5 eV (Cu $2p_{3/2}$) are assigned to the Cu^+ species, whereas those at 954.2 eV (Cu $2p_{1/2}$) and 934.4 eV (Cu $2p_{3/2}$) correspond to Cu^{2+} species. In addition, satellite features at 941.6 eV and 943.7 eV are of Cu^{2+} shake-up transitions [71,72], further confirming the coexistence of both oxidation states. The presence of Cu^+ on the membrane surface suggests a partial reduction of Cu^{2+}, likely promoted by redox-active functional groups present in the membrane matrix. The presence of electron-rich organic functionalities, including hydroxyl, carboxyl, and amide groups, in hPAN/PVPI$_3$/GO$_3$ contributes to its negative surface charge (Table 3) and potential for electron donation, which can promote the reduction of Cu^{2+} to Cu^+. Raji et al. [57] investigated the mechanisms of heavy metal removal by various adsorbents and determined that redox interactions could be one of the potential adsorption mechanisms. In a related study, Chen et al. [73] investigated the use of biomass composed of sewage sludge for the removal of Cr^{6+}. Their findings indicated that during the adsorption process there was a partial reduction of Cr^{6+} to Cr^{3+} due to the presence of carboxyl, amide, and hydroxyl groups within the biomass.

Regarding the high-resolution XPS of Pb (Fig. 5d), the peaks observed at biding energies of 143.4 eV and 138.5 eV correspond to Pb $4f_{5/2}$ and Pb $4f_{7/2}$, respectively [74], indicating the formation of Pb—O bonds [70,75]. This suggests the formation of coordination complexes between Pb^{2+} and oxygen-containing functional groups of hPAN/PVPI$_3$/GO$_3$ as corroborated by FT-IR.

CLSM, AFM, and SEM analyses were also performed to investigate the morphology of the pristine and loaded hPAN/PVPI$_3$/GO$_3$ membrane (Fig. 6). The confocal image of the hPAN/PVPI$_3$/GO$_3$ surface (Fig. 6a) showed a rough surface, attributed to the PVPI/GO layers onto the pristine polymer [14]. The hPAN/PVPI$_3$/GO$_3$ membrane loaded with Cr^{3+}/Cu^{2+}/Pb^{2+} also exhibited a rough surface. However, while the roughness of the pristine membrane was narrower and slenderer, the roughness of the loaded membrane was broader and more voluminous (Fig. 6b).

Upon closer examination of the confocal image of the membrane after adsorption (Fig. 6b), it becomes evident that the darker regions exhibit similar conformations as those observed in the hPAN/PVPI$_3$/GO$_3$ membrane before adsorption (Fig. 6a). Additionally, larger and more prominent rough areas, highlighted as lighter regions, are heterogeneously distributed across the membrane surface. This suggests the deposition of metal ions (Pb^{2+}, Cu^{2+}, Cu^+, and Cr^{3+}) onto the membrane. This interpretation is further supported by the 3D projections obtained from confocal analysis, which show that while the hPAN/PVPI$_3$/GO$_3$ membrane displays a relatively uniform surface, with moderate valleys and peaks, and an average surface thickness of 5.5 µm (Fig. 6 a1), the metal loaded membrane has a more heterogeneous topography, with more pronounced and widely distributed surface irregularities, and an increased average thickness of 7.1 µm (Fig. 6 b1). These findings suggest that the accumulation of metal ions contributes to the formation or accentuation of surface protrusions on the membrane.

The AFM analyses under liquid media (Fig. 6 a2-b2) provided results consistent with those obtained from CLSM confirming the deposition of metal ions on the hPAN/PVPI$_3$/GO$_3$ membrane. These analyses revealed the formation of larger and more prominent rough areas compared to those observed on the membrane before adsorption. Additionally, the AFM technique enabled the quantification of surface roughness through the mean square roughness (Sq) parameter, which showed an increase after adsorption. The Sq of the hPAN/PVPI$_3$/GO$_3$ membrane was 236 nm (Fig. 6a2), while the one of the metal loaded hPAN/PVPI$_3$/GO$_3$ membrane was 499 nm (Fig. 6a2). These findings may be attributed to

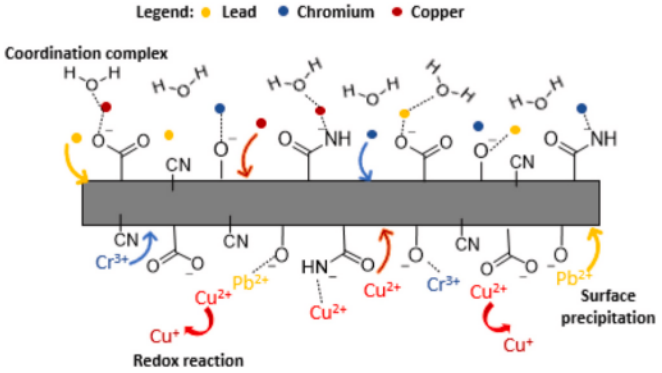

Fig. 7. Proposal mechanism for metals adsorption onto hPAN/PVPI$_3$/GO$_3$ membrane.

accumulation of metal ions on the surface of the material. Similar observations were reported by Milosavljević et al. [76], who employed hydrogels of chitosan, itaconic acid, and methacrylic acid for the adsorption of Cu^{2+} ions in batch mode. Topographic images of the hydrogels after the adsorption process indicated the agglomeration of grains on the surface, leading to increased roughness as the initial concentration of Cu^{2+} ions in the solution increased. Based on AFM results, the authors concluded that the toxic metal ions were both distributed on the surface and within the material.

The SEM-EDS mapping (Fig. 6a3) supports the findings from the CLSM and AFM analyses, which revealed the presence of metal ions through imaging and changes in the morphological parameters of the membranes. The SEM-EDS results showed that the membrane exhibited a rough surface and a uniform distribution of metal ions on its surface.

3.5.2. *hPAN/PVPI$_3$/GO$_3$ adsorption mechanism*

The hPAN/PVPI$_3$/GO$_3$ membrane, when applied in multicomponent systems for the removal of toxic metals (Cr^{3+}, Cu^{2+}, and Pb^{2+}), exhibited selective adsorption behavior and promising adsorption capacity. The adsorption mechanism of metal cations by the membrane was elucidated based on equilibrium modeling and post-adsorption spectroscopic and morphological analyses.

The equilibrium data fitted best to the BET and AD models, indicating multilayer adsorption involving both surface complexation and possible surface precipitation. This finding indicates that competitive adsorption in the multi-metal system promotes selective sorption, driven by the affinity of specific metal ions either for the membrane surface or for the surface of the precipitate.

Regarding the adsorbent/adsorbate interactions, FT-IR spectra of the loaded membranes showed shifts in the –OH (3436 → 3393 cm^{-1}) and –NH (1570 → 1547 cm^{-1}) stretching bands, as well as new absorption features at 3141/3042, 2924, and 2854 cm^{-1}, confirming coordination between the metal ions and oxygen- and nitrogen-containing groups. XPS analysis corroborated these interactions, evidencing the presence of Cr^{3+}, Cu^{2+}/Cu^{+}, and Pb^{2+} species. The partial reduction of Cu^{2+} to Cu^{+} suggests redox activity of surface functionalities, while Pb and Cr signals indicated coordination through O-containing groups such as hydroxyl and carbonyl. Morphological analyses (CLSM, SEM-EDS, and AFM) revealed a uniform metal distribution and an increase in surface roughness from 236 to 499 nm after adsorption, supporting multilayer deposition and complexation processes.

Overall, adsorption proceeds mainly *via* chemisorption through coordination complexes between the cations and the hPAN/PVPI$_3$/GO$_3$ membrane, coupled with surface precipitation and minor redox reactions (Fig. 7).

In summary, hPAN/PVPI$_3$/GO$_3$ membrane showed experimental maximum adsorption capacities of 6.42 mg g^{-1}, 23.2 mg g^{-1}, and 29.6 mg g^{-1} for Cr^{3+}, Cu^{2+}, and Pb^{2+}, respectively, when using a membrane mass of 0.01 g, at 298 K, and pH 5.5, with initial concentrations of 10 mg L^{-1} of Cr^{3+} and Pb^{2+}, and 20 mg L^{-1} of Cu^{2+}. Even in a multicomponent system, the membrane outperformed several other membranes reported in the literature for the removal of metal cations in unary systems (Table 6). These results highlight the high potential of hPAN/PVPI$_3$/GO$_3$ to remove toxic metals from water.

4. Conclusions

This study demonstrated that the hPAN/PVPI$_3$/GO$_3$ membrane exhibits high efficiency and selectivity for the removal of Cu^{2+}, Cr^{3+}, and Pb^{2+} ions in multicomponent systems, confirming its potential for environmental remediation applications. Under optimized conditions (pH 5.5 and 298 K), maximum adsorption capacities of 6.42, 23.2, and 29.6 mg g^{-1} were achieved for Cr^{3+}, Cu^{2+}, and Pb^{2+}, respectively. The adsorption behavior followed the pseudo-second-order kinetic and BET isotherm models, indicating chemisorption and multilayer adsorption processes influenced by competitive ion interactions. Spectroscopic and morphological analyses indicated that adsorption occurs mainly through coordination between the metal cations and oxygen- and nitrogen-containing groups, accompanied by multilayer adsorption and partial redox interactions. These synergistic processes increased the membrane's affinity and selectivity, particularly for Pb^{2+}, leading to high adsorption capacity and good reusability. Overall, the results

Table 6
Comparison of the solid concentration of hPAN/PVPI$_3$/GO$_3$ membrane with other membranes from the literature for the adsorption of Cu^{2+}, Cr^{3+}, and Pb^{2+}.

Membranes	Membrane mass (mg)	Metal ion	Adsorption system	Initial concentration (mg L^{-1})	pH	Temp. (K)	Calculated solid concentration ($q_{i.e}$, mg g^{-1})	Ref.
Cucurbit[8]uril sponge	100	Cr^{3+}	Binary	0.05–5	5.0	298	2.04*	[77]
Cucurbit[6]uril sponge	100	Cr^{3+}	Binary	0.05–5	5.0	298	9.44*	[77]
hPAN/PVPI$_3$/GO$_3$	**10**	**Cr^{3+}**	**Ternary**	**10**	**5.5**	**298**	**6.42**	**This work**
Polyvinylidene fluoride-attapulgite- fluorescent carbon dots composite membrane (PVDF/ATP-CDs)	–	Cu^{2+}	Unary	20	–	–	0.73	[78]
Cellulose acetate/polyethyleneimine blend membrane	15	Cu^{2+}	Unary	10	–	288	7.42	[79]
hPAN/PVPI$_3$/GO$_3$	**10**	Cu^{2+}	**Ternary**	**20**	**5.5**	**298**	**23.2**	**This work**
Thiol-functionalized cellulose nanofiber membrane	10	Pb^{2+}	Unary	20–400	4	298	22.0*	[80]
Chitosan/Silica Composite membrane	50	Pb^{2+}	Unary	220	7.0	298	57.6	[81]
hPAN/PVPI$_3$/GO$_3$	**10**	Pb^{2+}	**Ternary**	**10**	**5.5**	**298**	**29.6**	**This work**

* Langmuir maximum adsorption capacity.

demonstrate that the adsorption mechanism governs the membrane's efficiency in heavy metal remediation, confirming hPAN/PVPI₃/GO₃ as a promising and sustainable material for the remediation of heavy metal-contaminated waters.

CRediT authorship contribution statement

Tauany de Figueiredo Neves: Writing – review & editing, Writing – original draft, Visualization, Validation, Software, Project administration, Methodology, Investigation, Funding acquisition, Formal analysis, Data curation, Conceptualization. **Cláudia Batista Lopes:** Writing – review & editing, Visualization, Supervision, Software, Methodology, Investigation, Formal analysis, Data curation, Conceptualization. **Valmor Roberto Mastelaro:** Writing – review & editing, Visualization, Validation, Methodology, Funding acquisition, Formal analysis, Data curation. **Renato Falcão Dantas:** Writing – review & editing, Visualization, Validation, Supervision, Project administration, Funding acquisition. **Carlos Manuel Silva:** Writing – review & editing, Visualization, Validation, Supervision, Resources, Methodology, Funding acquisition, Formal analysis, Data curation, Conceptualization. **Patrícia Prediger:** Writing – review & editing, Visualization, Validation, Supervision, Resources, Project administration, Methodology, Funding acquisition, Formal analysis, Conceptualization.

Declaration of competing interest

The authors declare that they have no known competing financial interests or personal relationships that could have appeared to influence the work reported in this paper.

Acknowledgements

This study was financed, in part, by the National Council for Scientific and Technological Development (CNPq), Brazil (Grant No. 311419/2022-4 and 403211/2023-9), the Coordenação de Aperfeiçoamento de Pessoal de Nível Superior – Brasil (CAPES) – Finance Code 001, the Fundo de Apoio ao Ensino, à Pesquisa e à Extensão da Unicamp (FAEPEX), State University of Campinas, Brazil (Grant No. 2529/23 and 2207/23), the São Paulo Research Foundation (FAPESP), Brazil (Grant No. 2013/07296-2, 2019/25228-0, 2022/14834-0, and 2022/11525-6). "This work was developed within the scope of the project CICECO-Aveiro Institute of Materials, UIDB/50011/2020 (DOI 10.54499/UIDB/50011/2020), UIDP/50011/2020 (DOI 10.54499/UIDP/50011/2020) & LA/P/0006/2020 (DOI 10.54499/LA/P/0006/2020), financed by national funds through the FCT/MCTES (PIDDAC)." The authors are grateful to LNNano – National Nanotechnology Laboratory (CNPEM) for the support provided in Atomic Force Microscopy and Laser Scanning Confocal Microscopy analyses. We are grateful to Dra. Josiane Aparecida de Souza Vendemiatti for the SEM analyses carried out at the School of Technology at UNICAMP-Limeira. Cláudia B. Lopes thanks Fundação para a Ciência e a Tecnologia (FCT) for her researcher contract with reference 2021.03739.CEECIND/CP1659/CT0025 (DOI 10.54499/2021.03739.CEECIND/CP1659/CT0025). Thanks are also due to FCT/MCTES for the financial support to CERES (UIDB/00102/2020).

Appendix A. Supplementary data

Supplementary data to this article can be found online at https://doi.org/10.1016/j.molliq.2025.129055.

Data availability

Data will be made available on request.

References

[1] U.S. DEPARTMENT OF LABOR, Toxic Metals, Occupational Safety and Health Administration. https://www.osha.gov/toxic-metals, 2024.
[2] S. Rajendran, A.K. Priya, P. Senthil Kumar, T.K.A. Hoang, K. Sekar, K.Y. Chong, K. S. Khoo, H.S. Ng, P.L. Show, A critical and recent developments on adsorption technique for removal of heavy metals from wastewater-a review, Chemosphere 303 (2022) 135146, https://doi.org/10.1016/j.chemosphere.2022.135146.
[3] L. Yuan, J. Li, X. Wang, Q. Zhao, L. Li, K. Wang, G. Wang, Preparation of iron composite filler for PRB technology and its application in the removal of toxic metals(loids) from groundwater, J. Environ. Chem. Eng. 12 (2024) 112570, https://doi.org/10.1016/j.jece.2024.112570.
[4] F.S. Hoseinian, S. Ramshini, B. Rezai, E. Kowsari, M. Safari, Toxic heavy metal ions removal from wastewater by ion flotation using a nano collector, Miner. Eng. 204 (2023) 108380, https://doi.org/10.1016/j.mineng.2023.108380.
[5] H. Liu, W. Zeng, M. He, Distribution, sources, contamination, and risks of toxic metals in Zijiang River, a typical tributary of the midstream of the Yangtze River in China, J. Environ. Sci. (China) (2024) 1–14, https://doi.org/10.1016/j.jes.2023.12.030.
[6] C.B. Gundersen, E. Yakushev, P. Terentjev, N. Kashulin, V. Korobov, N. Frolova, A. Romanov, U. Jermilova, A. Lokhov, I. Miskevich, E. Kotova, E.H. Steindal, H. F. Veiteberg Braaten, Mercury in the Barents region – river fluxes, sources, and environmental concentrations, Environ. Pollut. 333 (2023) 122055, https://doi.org/10.1016/j.envpol.2023.122055.
[7] A. Iqbal, E. Cevik, A. Mustafa, T.F. Qahtan, M. Zeeshan, A. Bozkurt, Emerging developments in polymeric nanocomposite membrane-based filtration for water purification: a concise overview of toxic metal removal, Chem. Eng. J. 481 (2024) 148760, https://doi.org/10.1016/j.cej.2024.148760.
[8] R. Budania, S. Dangayach, A comprehensive review on permeable reactive barrier for the remediation of groundwater contamination, J. Environ. Manag. 332 (2023) 117343, https://doi.org/10.1016/j.jenvman.2023.117343.
[9] E.A. Rodrigues, D.S. Violin, V.R. Mastelaro, T. de Figueiredo Neves, P. Prediger, Removal of propranolol by membranes fabricated with nanocellulose/proanthocyanidin/modified tannic acid: the influence of chemical and morphologic features and mechanism study, Int. J. Biol. Macromol. 256 (2024) 128268, https://doi.org/10.1016/J.IJBIOMAC.2023.128268.
[10] H. Sharma, N. Rana, J. Sarwan, J.C. Bose, M. Devi, R. Chugh, Nano-material for waste water treatment, Mater. Today Proc. (2023), https://doi.org/10.1016/J.MATPR.2023.02.258.
[11] J. Xie, K. Li, N.Z.B. Nizzar, H. Meng, X. Mao, Quantitative nanoscopic imaging of adsorbent-aggregation-state dependent molecular binding cooperativity, J. Mater. Chem. A 12 (2024) 23697–23711, https://doi.org/10.1039/D4TA02208D.
[12] S. Biswas, A. Johri, A. Pal, New-Age Nano Adsorbents for Water Purification, Nanomater, Air Water Purif, 2024, pp. 1–25, https://doi.org/10.1002/9783527838059.ch1.
[13] F. Damiri, S. Andra, N. Kommineni, S.K. Balu, R. Bulusu, A.A. Boseila, D.O. Akamo, Z. Ahmad, F.S. Khan, M.H. Rahman, M. Berrada, S. Cavalu, Recent advances in adsorptive nanocomposite membranes for heavy metals ion removal from contaminated water: a comprehensive review, Materials (Basel). 15 (2022), https://doi.org/10.3390/ma15155392.
[14] T. de F. Neves, C.B. Lopes, V.R. Mastelaro, R.F. Dantas, C.M. Silva, P. Prediger, Toxic metals removal by new membranes based on graphene oxide and a cationic polymer: influence of chemical and morphological aspects, Chem. Eng. J. 498 (2024) 155496, https://doi.org/10.1016/j.cej.2024.155496.
[15] W.S. Hummers, R.E. Offeman, Preparation of graphitic oxide, J. Am. Chem. Soc. 80 (1958) 1339, https://doi.org/10.1021/ja01539a017.
[16] N. Bicak, M. Gazi, Quantitative quaternization of poly(4-vinyl pyridine), J. Macromol. Sci. - Pure Appl. Chem. 40 (2003) 585–591, https://doi.org/10.1081/MA-120020865.
[17] M. Hu, B. Mi, Layer-by-layer assembly of graphene oxide membranes via electrostatic interaction, J. Membr. Sci. 469 (2014) 80–87, https://doi.org/10.1016/j.memsci.2014.06.036.
[18] G. Won, Y.M. Lee, Y.T. Lee, Pervaporation of water-ethanol through Polyion complex membrane from Polyacrylonitrile and poly(vinyl pyridine), Polym 15 (1991) 625–631.
[19] P. Sharma, S. Tripathi, D. Purchase, R. Chandra, Integrating phytoremediation into treatment of pulp and paper industry wastewater : field observations of native plants for the detoxification of metals and their potential as part of a multidisciplinary strategy, J. Environ. Chem. Eng. 9 (2021) 105547, https://doi.org/10.1016/j.jece.2021.105547.
[20] P. Sharma, H.M.N. Iqbal, R. Chandra, Case studies in chemical and environmental engineering evaluation of pollution parameters and toxic elements in wastewater of pulp and paper industries in India : a case study, Case Stud. Chem. Environ. Eng. 5 (2022) 100163, https://doi.org/10.1016/j.cscee.2021.100163.
[21] S. Lagergren, About the theory of so-called adsorption of soluble substances, K. Sven. VETENSKAPSAKADEMIENS Handl. 24 (1898) 1–39.
[22] Y.S. Ho, G. McKay, Pseudo-second order model for sorption processes, Process Biochem. 34 (1999) 451–465, https://doi.org/10.1016/S0032-9592(98)00112-5.
[23] Walter J. Weber, J. Carrell Morris, Kinetics of adsorption on carbon from solution, J. Sanit. Eng. Div. 89 (1963) 31–60.
[24] J. Wang, C.P. Huang, H.E. Allen, D.K. Cha, D.W. Kim, Adsorption characteristics of dye onto sludge particulates, J. Colloid Interface Sci. 208 (1998) 518–528, https://doi.org/10.1006/jcis.1998.5875.
[25] R.J. Aguerre, C. Suarez, P.E. Viollaz, New BET type multilayer sorption isotherms. Part I: theoretical derivation of the model, LWT Food Sci. Technol. 22 (1989) 188–191.

[26] F.S. Pantuso, M.P. Tolaba, R.J. Aguerre, A BET approach to multilayer adsorption in swelling products, J. Food Eng. 122 (2014) 68–71, https://doi.org/10.1016/j.jfoodeng.2013.07.036.
[27] G.L. Aranovich, M.D. Donohue, A new approach to analysis of multilayer adsorption, J. Colloid Interface Sci. 173 (1995) 515–520, https://doi.org/10.1006/jcis.1995.1353.
[28] G.L. Aranovich, M.D. Donohue, Multilayer adsorption of slightly soluble organic compounds from aqueous solutions, J. Colloid Interface Sci. 178 (1996) 764–769, https://doi.org/10.1006/jcis.1996.0175.
[29] S. Al-Meer, A. El-Shafie, K. Al-Saad, H. Dolas, Effective Removal of Methylene Blue from Wastewater Using NiO and Triethanolamine-Modified Electrospun Polyacrylonitrile Nanofiber, Process 13 (2025) 2032, https://doi.org/10.3390/PR13072032.
[30] Y. Xie, X. Wang, H. Li, T. Wang, W. Feng, J. Li, PAN/TiO2 ultrafiltration membrane for enhanced BSA removal and antifouling performance, Catalysts 13 (2023) 1320, https://doi.org/10.3390/CATAL13101320.
[31] F. Panagiotou, I. Zuburtikudis, H. Abu Khalifeh, E. Nashef, V. Deimede, GO and surfactant assisted regulation of polyamide nanofiltration membranes for improved separation performance, Sep. Purif. Technol. 352 (2025) 128220, https://doi.org/10.1016/J.SEPPUR.2024.128220.
[32] Y. Pang, C. Zhao, Y. Li, Q. Li, X. Bayongzhong, D. Peng, T. Huang, Cadmium adsorption performance and mechanism from aqueous solution using red mud modified with amorphous MnO2, Sci. Rep. 12 (2022) 1–18, https://doi.org/10.1038/s41598-022-08451-2.
[33] G. Amrutha, C.R. Jeppu, B. Girish, K. Prabhu, Mayer, multi-component adsorption isotherms: review and modeling studies, Environ. Process. 10 (2023) 38, https://doi.org/10.1007/s40710-023-00631-0.
[34] G. Dobrescu, F. Papa, D. Culita, I. Balint, N.I. Ionescu, Cerofolini's Model and the Fractal Adsorption Isotherms, Fractal Fract 7 (2023) 262, https://doi.org/10.3390/FRACTALFRACT7030262.
[35] C. Yin, Y. Zhang, Y. Tao, X. Zhu, Competitive adsorption behavior and adsorption mechanism of limestone and activated carbon in polymetallic acid mine water treatment, Sci. Rep. 14 (2024) 23561, https://doi.org/10.1038/s41598-024-74240-8.
[36] F. Ebrahimzadeh, A. Akbari, Investigation the adsorption mechanisms, chemical resistance and mechanical strength of the synthesized chitosan/activated carbon composite in methylene blue removal, Sci. Report. 15 (2025) 37820, https://doi.org/10.1038/s41598-025-21734-8.
[37] K. Saito, M. Morita, T. Okada, R. Ploy Wijitwongwan, M. Ogawa, Designed functions of oxide/hydroxide nanosheets via elemental replacement/doping, Chem. Soc. Rev. 53 (2024) 10523–10574, https://doi.org/10.1039/D4CS00339J.
[38] K.S. Obayomi, S.Y. Lau, M.K. Danquah, J. Zhang, T. Chiong, O.V. Obayomi, L. Meunier, M.M. Rahman, A response surface methodology approach for the removal of methylene blue dye from wastewater using sustainable and cost-effective adsorbent, Process. Saf. Environ. Prot. 184 (2024) 129–150, https://doi.org/10.1016/J.PSEP.2024.01.106.
[39] Z. Niu, S. Zhang, M. Ma, Z. Wang, H. Zhao, Y. Wang, Synthesis of novel waste batteries-sawdust-based adsorbent via a two-stage activation method for Pb2+ removal, Environ. Sci. Pollut. Res. 26 (2018) 4730–4745, https://doi.org/10.1007/S11356-018-3883-0.
[40] R.R. Sheha, Preparation and performance of a novel composite as a reactive resin for copper retention, Chem. Eng. J. 213 (2012) 163–174, https://doi.org/10.1016/J.CEJ.2012.09.113.
[41] L. Liang, J. Wang, X. Tong, S. Zhang, Enhanced adsorptive removal of Cr(III) from the complex solution by NTA-modified magnetic mesoporous microspheres, Environ. Sci. Pollut. Res. 29 (2022) 45623–45634, https://doi.org/10.1007/S11356-022-19039-8.
[42] D. Zhao, Y. Zhang, C. Wu, Adsorption of Pb(II) ions by functionalized multi-walled carbon nanotubes MWCNTs-NH2, J. Hazard. Mater. Adv. 19 (2025) 100764, https://doi.org/10.1016/J.HAZADV.2025.100764.
[43] O. Hosseinkhani, A. Hamzehlouy, S. Dan, N. Sanchouli, M. Tavakkoli, H. Hashemipour, Graphene oxide/ZnO nanocomposites for efficient removal of heavy metal and organic contaminants from water, Arab. J. Chem. 16 (2023) 105176, https://doi.org/10.1016/j.arabjc.2023.105176.
[44] N. He, W. Li, H. Xu, A QICAR model for quantifying connection between metal ionic character and biosorption capacity of Pleurotus eryngii, Desalin. Water Treat. 52 (2014) 6519–6529, https://doi.org/10.1080/19443994.2013.815586.
[45] D.W. Smith, Ionic hydration enthalpies, J. Chem. Educ. 1 (1977) 1–3, https://pubs.acs.org/doi/abs/10.1021/ed054p540.
[46] V.J. Inglezakis, M.D. Loizidou, H.P. Grigoropoulou, Ion exchange of Pb2+, Cu2+, Fe3+, and Cr3+ on natural clinoptilolite: selectivity determination and influence of acidity on metal uptake, J. Colloid Interface Sci. 261 (2003) 49–54, https://doi.org/10.1016/S0021-9797(02)00244-8.
[47] M. Macena, H. Pereira, L. Cruz-Lopes, L. Grosche, B. Esteves, Competitive Adsorption of Metal Ions by Lignocellulosic Materials: A Review of Applications, Mechanisms and Influencing Factors 12 (2025) 70, https://doi.org/10.3390/SEPARATIONS12030070.
[48] D. Saha, H.A. Grappe, Adsorption properties of activated carbon fibers, Act. Carbon Fiber Text. (2017) 143–165, https://doi.org/10.1016/B978-0-08-100660-3.00005-5.
[49] P.M. Silva, N.G. Camparotto, T.F. Neves, K.T.G. Lira, V.R. Mastelaro, C.S.F. Picone, P. Prediger, Effective removal of basic dye onto sustainable chitosan beads : Batch and fixed-bed column adsorption, beads stability and mechanism, Sustain. Chem. Pharm. 18 (2020) 100348, https://doi.org/10.1016/j.scp.2020.100348.
[50] M.S. Akhtar, S. Ali, W. Zaman, Innovative adsorbents for pollutant removal: exploring the latest research and applications, Molecules 29 (2024) 1–37, https://doi.org/10.3390/molecules29184317.
[51] E. Leandro-Silva, A.R.F. Pipi, A.G. Magdalena, M. Piacenti-Silva, Study of simultaneous adsorption efficiency of metals using modified organic and synthetic adsorbents, Matéria (Rio Janeiro). 27 (2022) e20220033, https://doi.org/10.1590/1517-7076-RMAT-2022-0033.
[52] W.A. Al-Amrani, S.A. Onaizi, Adsorptive removal of heavy metals from wastewater using emerging nanostructured materials: a state-of-the-art review, Sep. Purif. Technol. 343 (2024) 127018, https://doi.org/10.1016/J.SEPPUR.2024.127018.
[53] S. Shimizu, N. Matubayasi, Understanding sorption mechanisms directly from isotherms, Langmuir 39 (2023) 6113–6125, https://doi.org/10.1021/ACS.LANGMUIR.3C00256.
[54] G. de V. Brião, M.G.C. da Silva, M.G.A. Vieira, K.H. Chu, Correlation of type II adsorption isotherms of water contaminants using modified BET equations, colloid Interface, Sci. Commun. 46 (2022) 100557, https://doi.org/10.1016/J.COLCOM.2021.100557.
[55] H.K. Agbovi, L.D. Wilson, Adsorption processes in biopolymer systems: fundamentals to practical applications, INC (2021), https://doi.org/10.1016/b978-0-12-820541-9.00011-9.
[56] G. de V. Brião, M.G. da Silva, M.G.A. Vieira, Expanded vermiculite as an alternative adsorbent for the dysprosium recovery, J. Taiwan Inst. Chem. Eng. 127 (2021) 228–235, https://doi.org/10.1016/J.JTICE.2021.08.022.
[57] Z. Raji, A. Karim, A. Karam, S. Khalloufi, Adsorption of heavy metals: mechanisms, kinetics, and applications of various adsorbents in wastewater remediation—a review, Waste 1 (2023) 775–805, https://doi.org/10.3390/waste1030046.
[58] M. Mariana, A.K. Abdul, E.M. Mistar, E.B. Yahya, T. Alfatah, M. Danish, M. Amayreh, Recent advances in activated carbon modification techniques for enhanced heavy metal adsorption, J. Water Process Eng. 43 (2021) 102221, https://doi.org/10.1016/J.JWPE.2021.102221.
[59] G. Enaime, A. Baçaoui, A. Yaacoubi, M. Lübken, Biochar for Wastewater Treatment—Conversion Technologies and Applications, Appl. Sci. 10 (2020) 3492, https://doi.org/10.3390/APP10103492.
[60] J.C. Bullen, C. Lapinee, L.A. Miller, F. Bullough, A.J. Berry, J. Najorka, G. Cibin, R. Vilar, D.J. Weiss, Spectroscopic (XAS, FTIR) investigations into arsenic adsorption onto TiO2/Fe2O3 composites: evaluation of the surface complexes, speciation and precipitation predicted by modelling, Results Surf. Interfaces 9 (2022) 100084, https://doi.org/10.1016/J.RSURFI.2022.100084.
[61] K.B.L. Borchert, C. Steinbach, B. Reis, U. Lappan, N. Gerlach, M. Mayer, S. Schwarz, D. Schwarz, Adsorption vs. surface precipitation of Cu2+ onto porous poly(melamine-co-formaldehyde) particles, Microporous Mesoporous Mater. 348 (2023) 112383, https://doi.org/10.1016/j.micromeso.2022.112383.
[62] S. Satyam, S. Patra, Innovations and challenges in adsorption-based wastewater remediation: a comprehensive review, Heliyon 10 (2024) e29573, https://doi.org/10.1016/J.HELIYON.2024.E29573.
[63] B. Rezai, E. Allahkarami, Desorption/regeneration of adsorbents and their performance, Sustain. Remediat. Technol. Emerg. Pollut. Aqueous Environ. (2024) 263–283, https://doi.org/10.1016/B978-0-443-18618-9.00021-8.
[64] X. Xia, F. Zhou, J. Xu, Z. Wang, J. Lan, Y. Fan, Z. Wang, W. Liu, J. Chen, S. Feng, Y. Tu, Y. Yang, L. Chen, H. Fang, Unexpectedly efficient ion desorption of graphene-based materials, Nat. Commun. 13 (2022) 1–7, https://doi.org/10.1038/s41467-022-35077-9.
[65] M. Iqbal, A. Saeed, S.I. Zafar, FTIR spectrophotometry, kinetics and adsorption isotherms modeling, ion exchange, and EDX analysis for understanding the mechanism of Cd2+ and Pb2+ removal by mango peel waste, J. Hazard. Mater. 164 (2009) 161–171, https://doi.org/10.1016/J.JHAZMAT.2008.07.141.
[66] N.K. Gondia, J. Priya, S.K. Sharma, Synthesis and physico-chemical characterization of a Schiff base and its zinc complex, Res. Chem. Intermed. 43 (2017) 1165–1178, https://doi.org/10.1007/s11164-016-2690-9.
[67] D. Cortés-Arriagada, N. Villegas-Escobar, S. Miranda-Rojas, A. Toro-Labbé, Adsorption/desorption process of formaldehyde onto iron doped graphene: a theoretical exploration from density functional theory calculations, Phys. Chem. Chem. Phys. 19 (2017) 4179–4189, https://doi.org/10.1039/c6cp07710b.
[68] D. Park, Y.S. Yun, J.M. Park, XAS and XPS studies on chromium-binding groups of biomaterial during Cr(VI) biosorption, J. Colloid Interface Sci. 317 (2008) 54–61, https://doi.org/10.1016/j.jcis.2007.09.049.
[69] S.R. Chowdhury, E.K. Yanful, A.R. Pratt, Chemical states in XPS and Raman analysis during removal of Cr(VI) from contaminated water by mixed maghemite-magnetite nanoparticles, J. Hazard. Mater. 235–236 (2012) 246–256, https://doi.org/10.1016/j.jhazmat.2012.07.054.
[70] V.V. Burungale, R.S. Devan, S.A. Pawar, N.S. Harale, V.L. Patil, V.K. Rao, Y.R. Ma, J.E. Ae, J.H. Kim, P.S. Patil, Chemically synthesized PbS nanoparticulate thin films for a rapid NO2 gas sensor, Mater. Sci. Pol. 34 (2016) 204–211, https://doi.org/10.1515/msp-2016-0001.
[71] H. Liu, J. Xie, P. Liu, B. Dai, Effect of cu+/Cu2+ ratio on the catalytic behavior of anhydrous nieuwland catalyst during dimerization of acetylene, Catalysts 6 (2016) 1–11, https://doi.org/10.3390/catal6080120.
[72] Z. Dan, Y. Yang, F. Qin, H. Wang, H. Chang, Facile fabrication of Cu2O Nanobelts in ethanol on Nanoporous cu and their Photodegradation of methyl Orange, Materials (Basel). 11 (2018), https://doi.org/10.3390/MA11030446.
[73] H. Chen, J. Dou, H. Xu, Removal of Cr(VI) ions by sewage sludge compost biomass from aqueous solutions: reduction to Cr(III) and biosorption, Appl. Surf. Sci. 425 (2017) 728–735, https://doi.org/10.1016/j.apsusc.2017.07.053.
[74] S.M. Maliyekkal, K.P. Lisha, T. Pradeep, A novel cellulose–manganese oxide hybrid material by in situ soft chemical synthesis and its application for the removal of Pb

(II) from water, J. Hazard. Mater. 181 (2010) 986–995, https://doi.org/10.1016/J.JHAZMAT.2010.05.112.
[75] H. Cai, Y. Sun, X. Zhang, L. Zhang, H. Liu, Q. Li, T. Bo, D. Zhou, C. Wang, J. Lian, Reduction Temperature-Dependent Nanoscale Morphological Transformation and Electrical Conductivity of Silicate Glass Microchannel Plate, Mater 12 (2019) 1183, https://doi.org/10.3390/MA12071183.
[76] N.B. Milosavljević, M.D. Ristić, A.A. Perić-Grujić, J.M. Filipović, S.B. Štrbac, Z. L. Rakočević, M.T.K. Krušić, Removal of Cu2+ ions using hydrogels of chitosan, itaconic and methacrylic acid: FTIR, SEM/EDX, AFM, kinetic and equilibrium study, Colloids Surfaces A Physicochem. Eng. Asp. 388 (2011) 59–69, https://doi.org/10.1016/j.colsurfa.2011.08.011.
[77] L.R.R. Souza, R.S. Cicolani, B.E.S. de Freitas, G.L. Floriano, M.L. de Oliveira, A.G. S. de Oliveira Filho, M.A.M.S. da Veiga, G.J.F. Demets, Polyurethane sponges bearing cucurbituril adsorb Cr(III) and Pb(II) ions from contaminated water samples, Environ. Sci. Pollut. Res. 31 (2024) 29749–29762, https://doi.org/10.1007/S11356-024-33184-2/FIGURES/1.
[78] H. Zhao, D. Zhang, H. Sun, Y. Zhao, M. Xie, Adsorption and detection of heavy metals from aqueous water by PVDF/ATP-CDs composite membrane, Colloids Surfaces A Physicochem. Eng. Asp. 641 (2022) 128573, https://doi.org/10.1016/j.colsurfa.2022.128573.
[79] Z. Chen, M. Deng, Y. Chen, G. He, M. Wu, J. Wang, Preparation and performance of cellulose acetate/polyethyleneimine blend microfiltration membranes and their applications, J. Membr. Sci. 235 (2004) 73–86, https://doi.org/10.1016/j.memsci.2004.01.024.
[80] H.Y. Choi, J.H. Bae, Y. Hasegawa, S. An, I.S. Kim, H. Lee, M. Kim, Thiol-functionalized cellulose nanofiber membranes for the effective adsorption of heavy metal ions in water, Carbohydr. Polym. 234 (2020) 115881, https://doi.org/10.1016/j.carbpol.2020.115881.
[81] N. Rosdi, M.N.M. Sokri, N.M. Rashid, M.S. Che Chik, M.S. Musa, Chitosan/silica composite membrane: adsorption of Lead(II) ion from aqueous solution, J. Appl. Membr, Sci. Technol. 23 (2018) 63–72, https://doi.org/10.11113/amst.v23n1.141.